



# High-resolution $^{10}\text{Be}$ and paleomagnetic recording of the last polarity reversal in the Chiba composite section: Age and dynamics of the Matuyama–Brunhes transition



Quentin Simon<sup>a,\*</sup>, Yusuke Suganuma<sup>b,c</sup>, Makoto Okada<sup>d</sup>, Yuki Haneda<sup>d</sup>, ASTER Team<sup>a,1</sup>

<sup>a</sup> CEREGE UM34, Aix Marseille Univ, CNRS, IRD, INRA, Coll France, 13545 Aix en Provence, France

<sup>b</sup> National Institute of Polar Research, 10-3 Midoricho, Tachikawa, Tokyo 190-8518, Japan

<sup>c</sup> Department of Polar Science, SOKENDAI, 10-3 Midoricho, Tachikawa, Tokyo 190-8518, Japan

<sup>d</sup> Department of Earth Sciences, Ibaraki University, 2-1-1 Bunkyo, Mito, Ibaraki 310-8512, Japan

## ARTICLE INFO

### Article history:

Received 30 November 2018  
Received in revised form 25 April 2019  
Accepted 1 May 2019  
Available online 21 May 2019  
Editor: B. Buffett

### Keywords:

authigenic  $^{10}\text{Be}/^9\text{Be}$  ratio  
relative paleointensity  
virtual geomagnetic poles  
Matuyama–Brunhes polarity transition  
Chiba composite section  
GSSP stratotype

## ABSTRACT

We present new magnetic (direction and relative paleointensity) and beryllium isotope ( $^{10}\text{Be}$ ,  $^9\text{Be}$  and  $^{10}\text{Be}/^9\text{Be}$  ratio) results covering the last geomagnetic reversal, i.e., the Matuyama–Brunhes transition (MBT), from the Chiba composite section (CbCS), east-central Japan. The very high sedimentation rates ( $>90$  cm/ka) of the studied site, a candidate site for the global boundary stratotype section and point (GSSP) of the Lower–Middle Pleistocene boundary, allow the acquisition of a dataset of exceptional resolution. Coupled cosmogenic  $^{10}\text{Be}$  and magnetic results measured on the same samples demonstrate that the magnetization acquisition conserved the timing of rapid geomagnetic features, allowing accurate paleomagnetic interpretations. A polarity switch (PS) capturing most of the angular deviation occurring between 771.9 and 773.9 ka was followed by a directional instability rebound (IC1) until 768.5 ka. This sequence with 5.4 ka duration was characterized by a weak dipole field as low as  $2.3 \pm 0.3 \times 10^{22}$  Am<sup>2</sup>. Four rapid episodes of directional instabilities preceding and following the PS–IC1 phase completed the reversal sequence. The asymmetry observed between the long-term dipole decay and sharp recovery, and rapid oscillations ( $<1$  ka) demonstrate the complex transitional field behavior during dipole moment low before reestablishment of the full polarity state. Our observations reinforce the fact that most reversal records do not integrate the full field behavior associated with the geodynamo action. Although this poses problems for understanding the underlying physical processes that produce reversals, it does not hamper stratigraphic correlations among most geologic records.

© 2019 The Authors. Published by Elsevier B.V. This is an open access article under the CC BY-NC-ND license (<http://creativecommons.org/licenses/by-nc-nd/4.0/>).

## 1. Introduction

Geomagnetic polarity reversals are the most severe expression of geomagnetic field variations generated and sustained by geodynamo action (Merrill and McFadden, 1999). Despite the large database available, interpretations of reversal records are controversial due to sporadic volcanic sequences and limited constraints on the processes involved in sediment magnetization (Love and Mazaud, 1997; Coe and Glen, 2004; Valet and Fournier, 2016). Paleomagnetic data from transitional lava flows provide important hints about field characteristics, but these are hardly helpful for constraining the complete dynamical sequence of reversals (e.g., Jarboe et al., 2011; Valet et al., 2012; Balbas et al.,

2018). For continuously deposited sediments, low-to-moderate resolution paleomagnetic records (defined by typical sedimentation rates of  $<10$  cm/ka) are associated with (post-)detrital remanent magnetization (pDRM) uncertainties and with smearing and smoothing of the magnetic signal, preventing accurate recording of rapid geomagnetic variations (e.g., Roberts and Winklhofer, 2004; Suganuma et al., 2011; Valet et al., 2016). High sedimentation rate records (10 to 20 cm/ka) reveal complex reversal dynamics but are limited to a few records in the North Atlantic (e.g., Channell, 2017). In addition, the rare reversal records from sites with higher sedimentation rates ( $>20$  cm/ka) are often associated with variable sedimentation patterns or complex diagenetic processes (e.g., complete or partial remagnetization, chemical transformations of magnetic minerals) that call into question their ability to properly record geomagnetic field changes over transitional periods characterized by weak fields (e.g., Quidelleur et al., 1992; Roberts et al., 2010; Sagnotti et al., 2010, 2016; Evans and Muxworthy, 2018).

\* Corresponding author.

E-mail address: [simon@cerege.fr](mailto:simon@cerege.fr) (Q. Simon).

<sup>1</sup> Georges Aumâtre, Didier L. Bourlès, Karim Keddadouche.

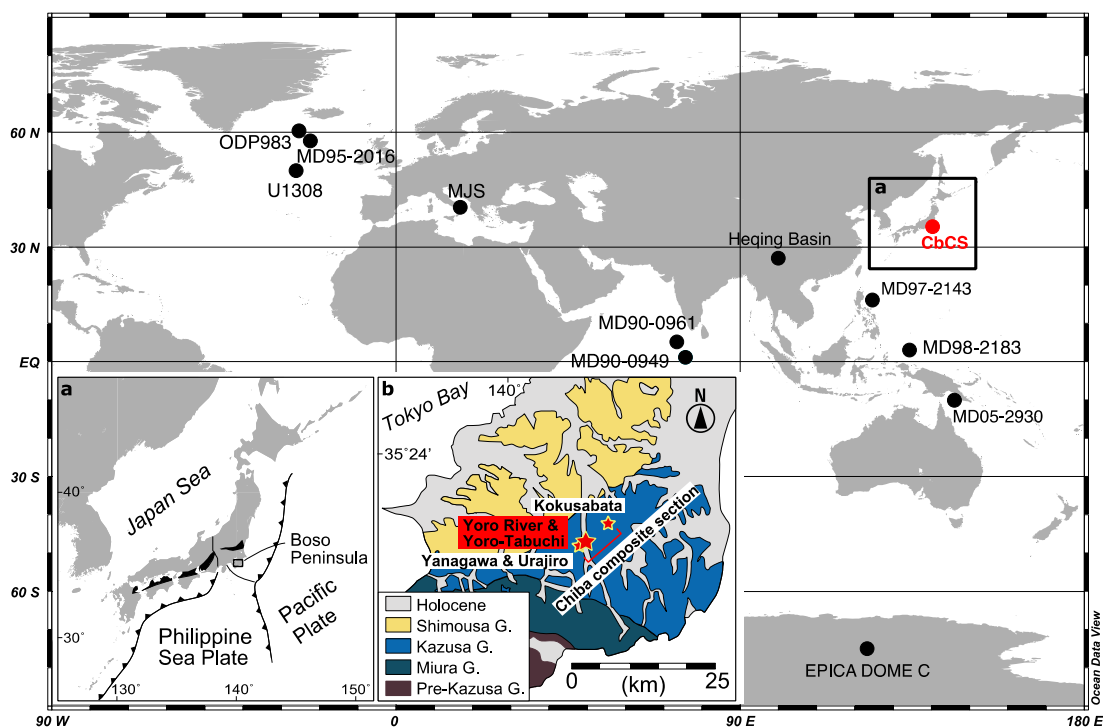


**Fig. 1.** Geographic location of the Chiba composite section (CbCS, red dot) along with marine and glacial records discussed in the text (black dots). These references include Montalbano Jonico (Simon et al., 2017; Nomade et al., 2019); MD95-2016, MD95-0949, and MD98-2183 (Simon et al., 2018b; Valet et al., 2019); MD90-0961 (Valet et al., 2014); Epica Dome C (EDC) (Raisbeck et al., 2006); MD97-2143 (Suganuma et al., 2010; Simon et al., 2018a); MD05-2930 (Ménabréaz et al., 2014; Simon et al., 2016a); and Heqing paleolake (Du et al., 2018). The precise location of the CbCS and a geological map of the Boso Peninsula are provided in boxes (a) and (b), respectively. Samples used in this study are from the Yoro River and Yoro-Tabuchi sections (highlighted in red in b). (For interpretation of the colors in the figure(s), the reader is referred to the web version of this article.)

Therefore, sediment records provide invaluable information about long-term geomagnetic field behavior, but the question of whether they are capable of recording rapid variations with adequate precision has generated much discussion over the years, restraining accurate interpretations of reversal dynamics (i.e., simple or complex?) and their underlying physical processes. It also casts doubt on the ability to make accurate comparisons between paleomagnetic reversal records from low, moderate, and high sediment deposition rate sites.

Along with transient directions, all reversals are characterized by a collapse of the geomagnetic dipole moment (GDM). This large-scale feature of the dipole field must be captured correctly by models to understand (and possibly predict) its occurrence and detailed behavior (Buffett, 2015; Morzfeld et al., 2017). Paleofield intensity can be reconstructed from sediments using a relative paleointensity (RPI) index (e.g., Tauxe, 1993; Valet, 2003) and cosmogenic nuclide beryllium-10 ( $^{10}\text{Be}$ ) measurements (e.g., Lal and Peters, 1967; Raisbeck et al., 1985). Paleomagnetic measurements allow reconstruction of the total paleomagnetic vector, including directions, but they are associated with DRM uncertainties (e.g., variable lock-in depth) and likely contain intricate contributions of the dipole and non-dipole fields during transitions (Leonhardt and Fabian, 2007; Valet and Fournier, 2016). Measurement of  $^{10}\text{Be}$  concentrations in sedimentary sequences permits the reconstruction of past production rates after environmental components have been screened out, thus providing an independent proxy for GDM variations and field instabilities (e.g., Simon et al., 2016a). The two complementary methods can be employed simultaneously to evaluate their respective limitations, obtain reliable reversal records, and help address two fundamental questions: (1) Is DRM capable of accurately recording the dynamics of rapid geomagnetic field changes during reversals? (2) Do geomagnetic field records during polarity transitions present similar and globally synchronized signatures?

In this study, we present new paleomagnetic and authigenic  $^{10}\text{Be}$ ,  $^9\text{Be}$ , and  $^{10}\text{Be}/^9\text{Be}$  ratio results covering the last geomagnetic reversal, i.e., the Matuyama–Brunhes transition (MBT), from the Chiba composite section (CbCS), a candidate host of the global boundary stratotype section and point (GSSP) of the Lower–Middle Pleistocene boundary. The very high sedimentation rates, more than 10 times higher than those of typical marine sediment records, of the studied site allow the acquisition of a dataset of exceptional resolution. Cosmogenic  $^{10}\text{Be}$  and paleomagnetic results obtained from the same samples are compared to extract accurate field values (amplitudes, durations, rates) during the MBT. These features, which may provide constraints on geomagnetic models and assist global correlation of paleo-records, are then discussed.

## 2. Geological settings and chronology

The Yoro-Tabuchi and Yoro River sections form the main part of the CbCS in the Kokumoto Formation of the Kazusa Group in the southeastern Japanese islands (Suganuma et al., 2018) (Fig. 1). The sections represent an expanded and well-exposed sedimentary succession characterized by stable deposition of bioturbated silty beds. Marine oxygen isotope records reveal continuous deposition from Marine Isotope Stage (MIS) 21 to MIS 18 with glacial and interglacial cycles corresponding to sandstone- and siltstone-dominated units, respectively (Okada and Niitsuma, 1989; Pickering et al., 1999). Widespread tephra beds originating from regional volcanic activity provide straightforward correlations of distant sections. Among those tephra layers, the Ontake–Byakubi tephra (Byk-E hereafter) bed, consisting of white pumiceous fine ash with 1 to 5 cm thickness (Kazaoka et al., 2015) originating from the Ontake volcano in the central part of the Japanese archipelago (Takeshita et al., 2016), provides the reference stratigraphic level (i.e., 0 m), which is easily identified in the CbCS.

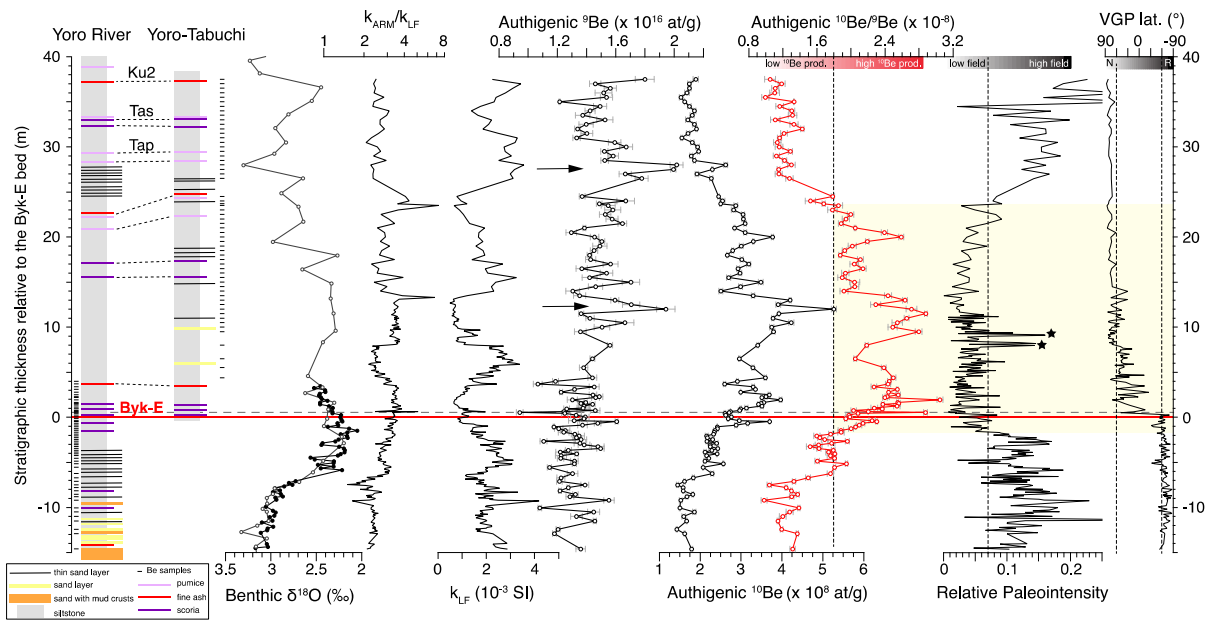


**Fig. 2.** Geochemical and magnetic results from the Chiba composite section (CbCS). Stratigraphic correlations between the Yoro River and Yoro-Tabuchi sections are provided on the left hand side (see legend). Samples for Be measurements are shown by black horizontal lines. The benthic  $\delta^{18}\text{O}$  data are from Suganuma et al. (2015) (empty dots) and Okada et al. (2017) (full dots).  $k_{\text{ARM}}/k_{\text{LF}}$  and  $k_{\text{LF}}$  provide information on magnetic mineralogy (see text).

A  $\delta^{18}\text{O}$  stratigraphy from benthic foraminifera was first established by Suganuma et al. (2015) and subsequently improved by Okada et al. (2017) and Suganuma et al. (2018). The CbCS  $\delta^{18}\text{O}$  record was tuned to the sea level curve of Elderfield et al. (2012) in order to establish a chronological template. This astrochronology is controlled by a radioisotopic U–Pb zircon date of the Byk-E tephra of  $772.7 \pm 7.2$  ka (2 sigma analytical uncertainty; Suganuma et al., 2015). The resulting age model yields an average sedimentation rate of ca. 208 cm/ka for the whole CbCS (from 801 ka to 752 ka) and of ca. 89 cm/ka within the MBT interval (Suganuma et al., 2018).

### 3. Materials and methods

Rock samples for paleomagnetic and beryllium isotope analyses were collected from the Yoro River and Yoro-Tabuchi sections, located at  $35^{\circ}17.41'N$ ,  $140^{\circ}8.48' E$  and  $35^{\circ}17.41'N$ ,  $140^{\circ}8.49' E$ , respectively. An integrated stratigraphy of the CbCS based on detailed tephrostratigraphic and stratigraphic investigations (Suganuma et al., 2018) revealed that the Yoro-Tabuchi section is 3.5 m shorter than height of Okada et al. (2017). Cores with a diameter of 2.54 cm were collected at 310 horizons with a 10 to 50 cm stratigraphic interval and covering a 52-m succession across the Byk-E tephra bed using a portable engine drill. Each sample integrates about 30 yrs of field record during the MBT interval and up to 12 yrs using the average sedimentation rate. All core samples were oriented with a magnetic compass before being removed from the outcrop and cut into 2-cm-long specimens.

New magnetic measurements on samples from the upper part of the Yoro-Tabuchi section were performed to complete the detailed paleomagnetic study of Okada et al. (2017). Low-field magnetic susceptibility was measured on all specimens using a Kappridge susceptibility meter at Ibaraki University. The natural remanent magnetization (NRM) was measured using a three-axis cryogenic magnetometer (2G SRM-760R) installed in a magnetically shielded room at the National Institute of Polar Research and also partly measured using a two-axis cryogenic magnetometer (2G SRM-750R) in a magnetically shielded room at Ibaraki University. Anhysteretic remanent magnetization (ARM) was acquired in a 0.03-mT DC field with an 80-mT AF using the SRM-760R

magnetometer. Characteristic remanent magnetization (ChRM) directions were calculated after a hybrid demagnetization method, i.e., 5- to 10-mT increments up to 50–60 mT alternating field demagnetization (AFD) after 300 °C thermal demagnetization (ThD) to remove secondary low-temperature components. The RPI index was calculated by ARM normalization using results of the hybrid demagnetization method (see Okada et al., 2017, for details).

Samples for beryllium isotopic analysis were sub-sampled from the paleomagnetic samples following the completion of magnetic measurements to provide direct results for comparison and avoid any sampling bias. The analyses were carried out at the CEREGE National Cosmogenic Nuclides Laboratory (LN2C, France) according to the chemical procedure established by Bourlès et al. (1989) and revised by Simon et al. (2016b). Authigenic  $^{10}\text{Be}$  and its stable isotope  $^9\text{Be}$  were extracted from  $\sim 1$  g dry samples by soaking the samples in 20 ml of leaching solution (0.04 M hydroxylamine ( $\text{NH}_2\text{OH}\cdot\text{HCl}$ ) and 25% acetic acid) at  $95 \pm 5$  °C for 7 h. A 2-ml aliquot of the resulting leaching solution was sampled for measurement of the natural  $^9\text{Be}$  concentration using a graphite-furnace atomic absorption spectrophotometer (AAS) with a double beam correction (Thermo Scientific ICE 3400®). The remaining solution was spiked with 300  $\mu\text{l}$  of a  $9.8039 \times 10^{-4}$   $\text{g g}^{-1}$   $^9\text{Be}$  carrier before Be purification by chromatography to determine accurate  $^{10}\text{Be}$  sample concentrations from accelerator mass spectrometer (AMS) measurements of  $^{10}\text{Be}/^9\text{Be}$  ratios at the French AMS national facility ASTER (CEREGE).  $^{10}\text{Be}$  sample concentrations were calculated from the measured spiked  $^{10}\text{Be}/^9\text{Be}$  ratios normalized to the BeO STD-11 in-house standard ( $1.191 \pm 0.013 \times 10^{-11}$ ) (Braucher et al., 2015). Authigenic  $^{10}\text{Be}$  concentrations were decay-corrected using the  $^{10}\text{Be}$  half-life ( $T_{1/2}$ ) of  $1.387 \pm 0.012$  Ma (Chmeleff et al., 2010; Korschinek et al., 2010).

## 4. Results and interpretations

### 4.1. Beryllium

The authigenic  $^9\text{Be}$  concentrations vary from  $0.9$  to  $2.0 \times 10^{16}$   $\text{at g}^{-1}$ , with an average and standard deviation of  $1.4 \pm 0.2 \times 10^{16}$   $\text{at g}^{-1}$  (Fig. 2). Overall, higher  $^9\text{Be}$  concentrations and larger amplitude oscillations with two maxima at 12 and 28 m are observed

upward from 10 m. The authigenic  $^{10}\text{Be}$  (decay-corrected) concentrations vary from  $1.42$  to  $5.26 \times 10^8$  at  $\text{g}^{-1}$ , with an average and standard deviation of  $2.6 \pm 0.8 \times 10^8$  at  $\text{g}^{-1}$ . The  $^{10}\text{Be}$  concentrations are higher between  $-1$  and  $24$  m, peaking at  $12$  m above the ByK-E level. This  $^{10}\text{Be}$  spike also corresponds to a major  $^9\text{Be}$  increase likely associated with an increase of Be delivery probably attributable to higher denudation rates and/or scavenging rate enhancements related to specific climatic/oceanographic conditions. The authigenic  $^{10}\text{Be}/^9\text{Be}$  ratio (Be ratio hereafter) varies from  $0.98$  to  $3.05 \times 10^{-8}$ , with an average and standard deviation of  $1.8 \pm 0.5 \times 10^{-8}$ . The Be ratio profile is very similar with the  $^{10}\text{Be}$  record and presents a high and significant correlation coefficient of  $0.90$ . In contrast, no correlation exists between the Be ratio and its normalizer  $^9\text{Be}$  ( $r = -0.16$ ). It is also worth noting that the peak observed at  $12$  m in both Be isotope records and associated with an environmental imprint is averaged out by the Be ratio. Values above the mean occur between  $-2$  and  $24$  m (yellow banding in Fig. 2) and are characterized by 3 sub-peaks at  $1.95$ ,  $11.5$ , and  $20$  m, respectively. The sharp Be ratio peak observed immediately above the Byk-E tephra layer ( $0.55$  m) corresponds to a  $^9\text{Be}$  outlier (see dotted line in Fig. 2) and is not considered associated with a geomagnetic origin.

#### 4.2. Rock magnetism and paleomagnetism

Suganuma et al. (2015) and Okada et al. (2017) showed that the Yoro River and Yoro-Tabuchi sections are characterized by homogeneous rock-magnetic properties with reduced mineralogical and grain-size changes and that the remanence is carried by magnetite to Ti-poor titanomagnetite in the pseudo-single domain (PSD). These properties are summarized in Fig. 2 by the magnetic susceptibility ( $k_{\text{LF}}$ ) and ARM susceptibility normalized to magnetic susceptibility ( $k_{\text{ARM}}/k_{\text{LF}}$ ) used as magnetic concentration and grain-size proxies, respectively. The  $k_{\text{LF}}$  and  $k_{\text{ARM}}/k_{\text{LF}}$  records show that the magnetic oscillations are mainly driven by low-order concentration, grain size, or subtle mineralogical changes, fulfilling the criteria established for constructing a robust RPI index (Tauxe, 1993). The RPI shows a large interval of average low values ( $0.05 \pm 0.03$ ) spanning the depth interval of  $-2$  to  $24$  m (Fig. 2). It is significantly lower than the surrounding values ( $0.13 \pm 0.05$ ) and corresponds to the highest Be ratio values (and thus higher global production of atmospheric  $^{10}\text{Be}$ ). Both series are highly correlated ( $r = -0.81$ ), indicating a similar controlling mechanism. This low interval is only interrupted by two sharp peaks of higher RPI centered at  $8.2$  and  $9.2$  m (black stars in Fig. 2) that do not correspond to any magnetic property changes. The virtual geomagnetic poles (VGPs) exhibit transitional directions and large scatter ( $38.1 \pm 46.0^\circ$ ) within this low RPI/high Be ratio interval. Conversely, they define antipodal directions below ( $-67.5 \pm 9.9^\circ$ ; reverse) and above ( $77.5 \pm 4.8^\circ$ , normal) this interval (Fig. 2).

### 5. Discussion

#### 5.1. Recording of geomagnetic field variations over the MBT

Our new paleomagnetic results complete the record from Okada et al. (2017), which was limited to up to  $15$  m above the ByK-E tephra layer. The entire dataset now captures the field intensity recovery and directional stabilization in normal polarity and covers the whole reversal process from the late Matuyama (reverse) to the early Brunhes (normal). Complementary to the magnetic results, the Be ratio dataset provides an independent proxy of GDM variations, which allows better assessment of the recording of the geomagnetic field in the CbCS, because the production rate of atmospheric  $^{10}\text{Be}$  is controlled primarily by the GDM following an established inverse relationship (e.g., Poluianov et al., 2016).

This theoretical relationship has been verified in sediments and ice cores by the identification and quantification of  $^{10}\text{Be}$  overproduction episodes associated systematically with all reversals and geomagnetic excursions of the last  $2$  Ma (e.g., Frank et al., 1997; Carcaillet et al., 2004; Raisbeck et al., 2006; Thouveny et al., 2008; Suganuma et al., 2010; Ménabréaz et al., 2012; Valet et al., 2014; Horiuchi et al., 2016; Simon et al., 2016a, 2017, 2018a, 2018b; Du et al., 2018).

The excellent alignment of RPI decrease (increase) with Be ratio increase (decrease) shows that the magnetic measurements support a trustworthy recording of the dipole component of the field collapse/recovery associated with the MBT (Fig. 3a). The standardized records are particularly coherent, expressing similar variations during these intervals controlled by the dipole field (Fig. 3b). Our results further demonstrate that recording of the geomagnetic field occurred at, or immediately after, the time of sediment deposition, without any time delay, given the very short atmospheric journey of  $^{10}\text{Be}$  and its rapid scavenging rate at oceanic margins. Together with the very high sedimentation rates, this evidence of no or very little lock-in depth offset and post-depositional reworking supports the conclusion that the magnetization acquisition conserved the timing of rapid geomagnetic features, allowing high-resolution and accurate interpretations of the paleomagnetic record from the CbCS.

Figs. 3c–d show that the polarity transition (transitional VGPs defined using a conservative cut-off limit of  $\pm 45^\circ$ ) occurs within the first stage of the “intensity pit” (i.e., overall lower RPI values and higher Be ratio from  $-2$  to  $24$  m, Fig. 2). The sharp polarity switch (PS) between  $0.25$  and  $1.95$  m (VGP latitudes shifting from  $-80^\circ$  to  $71^\circ$ ) is followed by a large directional instability cluster (IC1, VGPs averaging  $34 \pm 19^\circ$ ) within the  $2$ – $5$  m interval, before stabilization to around the cut-off limit value from  $5$  to  $8$  m (IC2,  $45 \pm 14^\circ$ ). The PS–IC1 sequence from  $0.25$  to  $5$  m corresponds to the first low dipole intensity interval (Dip1) traced by both the RPI and  $^{10}\text{Be}$  proxies (Fig. 3d). Stable normal VGP latitudes between  $8$  and  $10$  m ( $72 \pm 5^\circ$ ) are followed by a minor VGP instability cluster (IC3,  $58 \pm 7^\circ$ ) that corresponds to a second dipole intensity low (Dip2) within the  $11$ – $14$  m interval. From  $8$  to  $19$  m, the slight discrepancies between the RPI and Be ratio datasets (Fig. 3b) could be attributable to either non-removed environmental contents on one and/or both proxies or interplay of dipolar and non-dipolar fields acting differently on both records. The RPI spikes observed within the  $8$ – $12.5$  m depth interval suggest a dominant non-dipolar signature on the paleomagnetic record during the interval of overall low dipole field intensity, as shown by higher Be ratio. Such an interval dominated by higher non-dipole energies (directly imprinting on the magnetic signal) and lower dipolar energy (maximum  $^{10}\text{Be}$  production rate) agrees with geomagnetic models and geodynamo simulations (Leonhard and Fabian, 2007; Olson et al., 2011) that show a similar state during times of transitional field (produced mainly by the reduction of dipole strength). Alternatively, these RPI spikes could also be associated with secondary magnetic overprints amplified during the period of overall weak magnetization of the primary dipolar component, but no rock-magnetic evidence supports such a scenario (Okada et al., 2017). Between  $14$  and  $19$  m, low RPI values together with VGPs indicating relatively stable normal polarity and reduced Be ratios suggest that the surface field geometry is dominated by a dipole component of low intensity until high dipole moment recovers from  $24$  m upward.

The CbCS record exhibits a VGP sequence represented by a rapid polarity switch followed by three instability clusters (IC1–IC2–IC3) showing progressive diminution of amplitude before stabilization in normal polarity (Fig. 3d). Prior to the reversal, two VGP deviations barely exceeding  $45^\circ$  are observed within the overall long-term interval of decreasing field intensity.

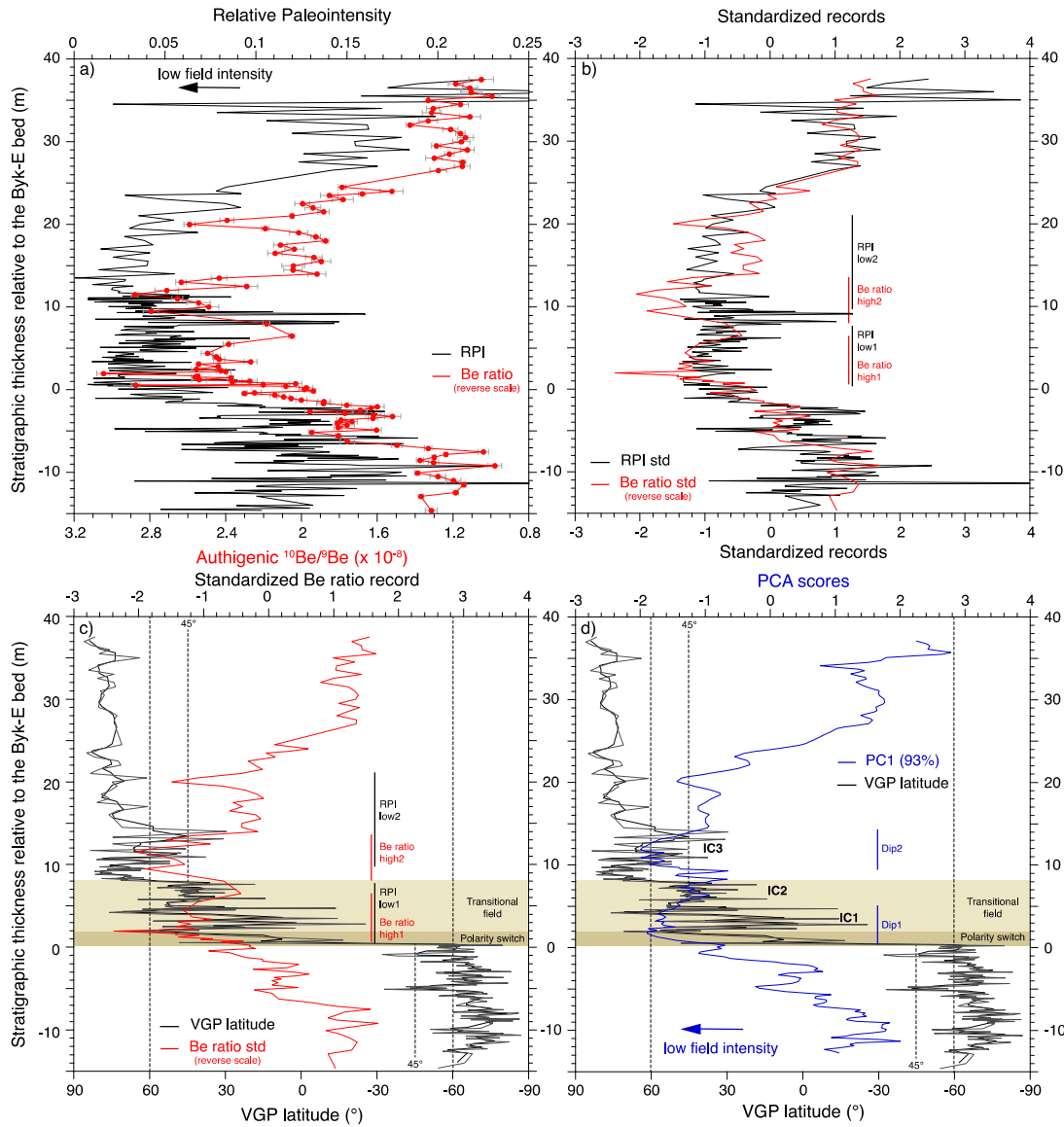


**Fig. 3.** Comparison between relative paleointensity (RPI), Be ratio, and virtual geomagnetic pole (VGP) variations. (a) Be ratio (red) and RPI (black) results. (b) Standardized RPI (black) and Be ratio (red) records. (c) VGP (gray) and standardized Be ratio (red) records. (d) First component (PC1) of the principal component analysis (PCA) performed on the RPI and Be ratio records (blue) and VGP changes (gray). (c–d) The black line corresponds to a 3-point running mean of the VGPs. The vertical dotted black lines correspond to the VGP cut-off limits ( $\pm 45^\circ$ ) used for defining the transitional field. The MBT is characterized by two phases: a polarity switch with VGPs shifting from  $-80^\circ$  to  $71^\circ$  between 0.25 and 1.95 m (dark brown banding), followed by transitional field values oscillating around  $39 \pm 14^\circ$  within the 1.95 to 8 m interval (light brown banding). This interval is characterized by two instability clusters (IC1 and IC2). The polarity switch and transitional field stages correspond to a first interval of dipole intensity low within the 0.25 to 5 m depth interval (Dip1). A third instability cluster (IC3) of lower amplitude corresponds to a second interval of dipole intensity low (11 to 14 m, Dip2).

## 5.2. Dynamics of geomagnetic variations over the MBT

Fig. 4 compares VGP latitude and dipole moment variations through time using the chronology of Suganuma et al. (2018). Chronological uncertainties associated with astronomical assumptions and age model construction can alter estimates of the absolute age, rate, and duration of geomagnetic variations within model uncertainties ( $\pm 5$  ka), but not their chronostratigraphic ordering or average magnitudes (time and amplitude). The normalized Be ratio record was calibrated in terms of dipole moment (DM) using the theoretical method presented in Simon et al. (2018b) and based on the  $^{10}\text{Be}$  production model of Poluianov et al. (2016). Overall high DM above  $10 \times 10^{22} \text{ Am}^2$ , which is proportionally similar to those observed during the late Holocene (Pavón-Carrasco et al., 2014), was reconstructed from either side of the “intensity pit” (which is averaged at  $3.9 \pm 1.2 \times 10^{22} \text{ Am}^2$  between  $-2$  and 24 m) that spans a 17 ka interval between 777 and 760 ka.

High DM values of  $12 \pm 1 \times 10^{22} \text{ Am}^2$  prevail until 790 ka and then decrease before values stabilize at  $6.5 \pm 0.5 \times 10^{22} \text{ Am}^2$  between 784 and 777 ka. This first-step halving is characterized by a rather constant rate of decrease of  $1.5 \times 10^{22} \text{ Am}^2/\text{ka}$ . This estimate corresponds to the decay rate observed over the last three millenniums (Genevey et al., 2008) and prior to the Laschamp excursion by independent high-resolution records (Laj and Kissel, 2015) and is about two times less rapid than the decay of the axial component of the dipole field observed in the last two centuries (Finlay et al., 2016). The significant VGP deviation observed at 784 ka is coherent with the occurrence of millennial scale instabilities over the  $\sim 33$  ka period preceding the MBT, as proposed by Balbas et al. (2018), and with an excursions precursor recorded in lava flows in Chile and Guadeloupe (Singer et al., 2018).

A second-step field collapse of similar rate observed between 777 and 772 ka is interrupted by a small break at mid-slope,

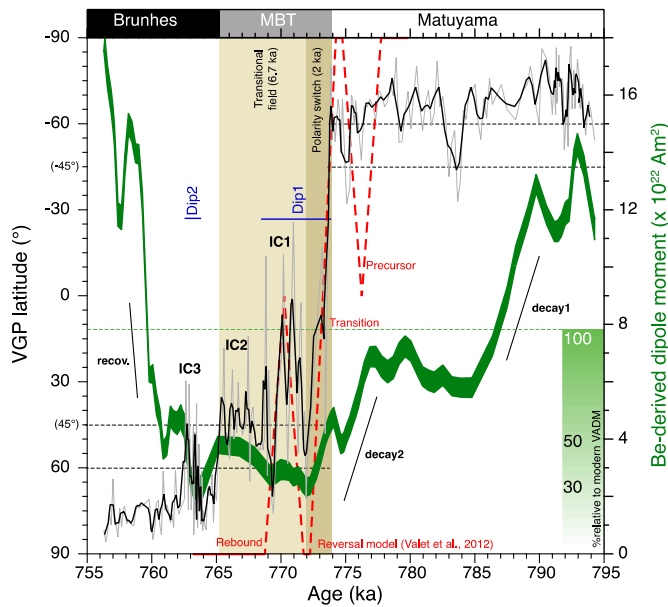


**Fig. 4.** Be ratio-derived dipole moment (BeDM; green curve) and VGP latitude (gray) over the MBT. The black line corresponds to a 3-point running mean of the VGPs. The polarity switches that explain most of the angular deviation span 2 ka (773.9 to 771.9 ka), but the transitional field prevails until 765.2 ka (IC1–IC2). The largest VGP deviations correspond to the Dip1 interval (773.7 to 767.4 ka). The green loading bar shows DM percent relative to present value. The results are compared with a schematic reversal path (red) illustrating the three-phase succession of reversal (precursor, transit, and rebound) described by Valet et al. (2012) from reversal volcanic sequences.

where the VGPs show a millennial deviation at 775 ka. The PS occurs during the second half of this field intensity decrease, over the interval of 773.9 to 771.9 ka (2 ka duration), with DM values waning from  $4.6 \pm 0.4$  to  $2.3 \pm 0.3 \times 10^{22} \text{ Am}^2$ . Most of the VGP deviation ( $128^\circ$  drift) occurs at the early stage of the PS phase within a 30 cm interval (0.25–0.55 m), representing about  $400 \pm 200$  yrs (773.8–773.4 ka). Such rapid VGP drift corresponds to the main directional change of a polarity reversal in a numerical dynamo (Olson et al., 2011) and is consistent with the identification of sub-millennial-length field oscillations during transitional intervals (Nowaczyk et al., 2012; Sagnotti et al., 2016; Chou et al., 2018). However, the uncertainty associated with the actual CbCS chronology precludes any robust interpretation at such centennial time scales. Overall, the 772–774 ( $\pm 5$ ) ka age range corresponds to the dating of the MBT from the most reliable marine sedimentary records (e.g., Tauxe et al., 1996; Channell et al., 2010; Channell, 2017; Simon et al., 2017, 2018b; Valet et al., 2019) and transitional lava flows (e.g., Ricci et al., 2018; Singer et al., 2018). Between 771.9 and 768.5 ka, large directional instabilities are contemporaneous with weak dipole field, average of  $2.7 \pm 0.2 \times 10^{22} \text{ Am}^2$ , indicating a significant non-dipolar contribution. Altogether, the succession of large directional instabilities and low DM values observed between 773.9 and 768.5 ka (PS and IC1,  $\text{DM} = 3.0 \pm 0.7 \times 10^{22} \text{ Am}^2$ ;  $\text{VGP} = 28.3 \pm 26.7^\circ$ ) agrees with the transition and rebound phases of the sequential reversal model proposed by Valet et al. (2012) from detailed volcanic records of reversals (Fig. 4). One can also tentatively associate the instability event at 775 ka with the precursor phase of the sequential reversal model, but its small amplitude deviation precludes any definitive conclusion. The identification of these successive phases and the nearly perfect timing agreement between our high-resolution record and the model can be seen as a posterior validation of the common duration assumption used by Valet et al. (2012) for correlating all transitional lava flows. It is also worth noting that this well-defined sequential reversal model occurs at the final stage of

a long-term unstable geodynamo period characterized by overall lower field intensity and the occurrence of one or several precursor events. These precursor events, defined by paleointensity lows and/or directional instabilities, are significantly lower than the precursor phase of the sequential reversal model (e.g., Hartl and Tauxe, 1996; Channell et al., 2009; Singer et al., 2005, 2018; Valet et al., 2014). Our results suggest that the precursor event dated at  $\sim 784$  ka is part of a continuum process associated with the dipole field strength reduction before the MBT (Fig. 4). Unfortunately, the limited time interval covered by our record prevents discussion of the older precursor event, dated at  $\sim 797$  ka, and its significance into the long-term geomagnetic field instability period preceding the reversal (Balbas et al., 2018).

Given the elements presented above, we are inclined to define the MBT by the PS and IC1 events during the low dipole moment spanning a 5.4 ka time interval (Dip1, 773.9–768.5 ka). However, the integration of the low-amplitude transitional VGP cluster observed until 765.2 ka (IC2 event at  $\sim 45^\circ$ ) extends the total transitional field interval, using a conservative definition, to a maximum 8.7 ka duration (Fig. 4). Whether the MBT should be defined by the PS phase alone (2 ka or less), the Dip1 low dipole intensity interval (PS–IC1, 5.4 ka), or the PS–IC1–IC2 succession (8.7 ka) depends largely on the definition of reversal (use of directional flip or intensity low) on the record resolution and is also likely site-dependent because of large non-dipole contribution during weak dipole periods (Clement, 2004; Valet et al., 2016). These elements are important because they add uncertainty to interpretations and chronostratigraphic correlations of reversals worldwide. As a matter of fact, rapid geomagnetic features are not recorded similarly between slower/faster sedimentation rate records, calling into question proper correlation of VGP paths from distinctive records. In Fig. 5a, we compare our VGP record to marine sequences of mid- to high-sedimentation rates, i.e., MD90-0961: 4.2 cm/ka (Valet et al., 2014), IODP Site U1308: 7.3 cm/ka (Channell et al., 2008), and ODP983, 13 cm/ka (Channell and Kleiven, 2000). The VGP records from CbCS and ODP983 are particularly well correlated, expressing a similar succession of instability events, especially for the PS and IC1 phases, but the VGP records from sites U1308 and MD90-0961 appear largely smoothed, time-averaging rapid instabilities of the transition sequence. VGP records of reversals from other high sedimentation rate sites (e.g., Okada and Niitsuma, 1989; Tric et al., 1991; Mazaud and Channell, 1999; Hyodo et al., 2006; Mazaud et al., 2009; Kusu et al., 2016; Channell, 2017; Kirscher et al., 2018) or lava flows (Jarboe et al., 2011; Mochizuki et al., 2011; Valet et al., 2012) also show a complex transitional field behavior with a similar succession of events and durations, whereas low sedimentation rate records always present smoothed profiles (Valet et al., 2016). The stochastic geomagnetic model of Buffett (2015) interprets such temporal complexity by the strength and structure of convective fluctuations in the outer core, explaining the increased variations of dipole generation during polarity transitions.

Immediately after the MBT, a dipole moment low (Dip2,  $2.4 \pm 0.4 \times 10^{22} \text{ Am}^2$ ) and small-amplitude instabilities cluster (IC3) are observed between 763.5 and 762.5 ka. This 1 ka duration instability event constitutes the last geomagnetic field ricochet before the dipole field stabilized in its new state. From 762 ka, the dipole field increases rapidly to very high DM values ( $14.3 \pm 1.7 \times 10^{22} \text{ Am}^2$ ), while directions are stabilized in normal polarity. The rate of this field recovery, average of  $5.3 \times 10^{22} \text{ Am}^2/\text{ka}$ , is three times higher than the rate of field decay, and DM reaches higher values than before the MBT. Similar field asymmetry between increasing and decreasing dipole strength changes framing reversals has already been observed from low-resolution global RPI stacks, sequences of superposed lava flows, and seafloor magnetization, and has been computed by geomagnetic models and reproduced by experimen-

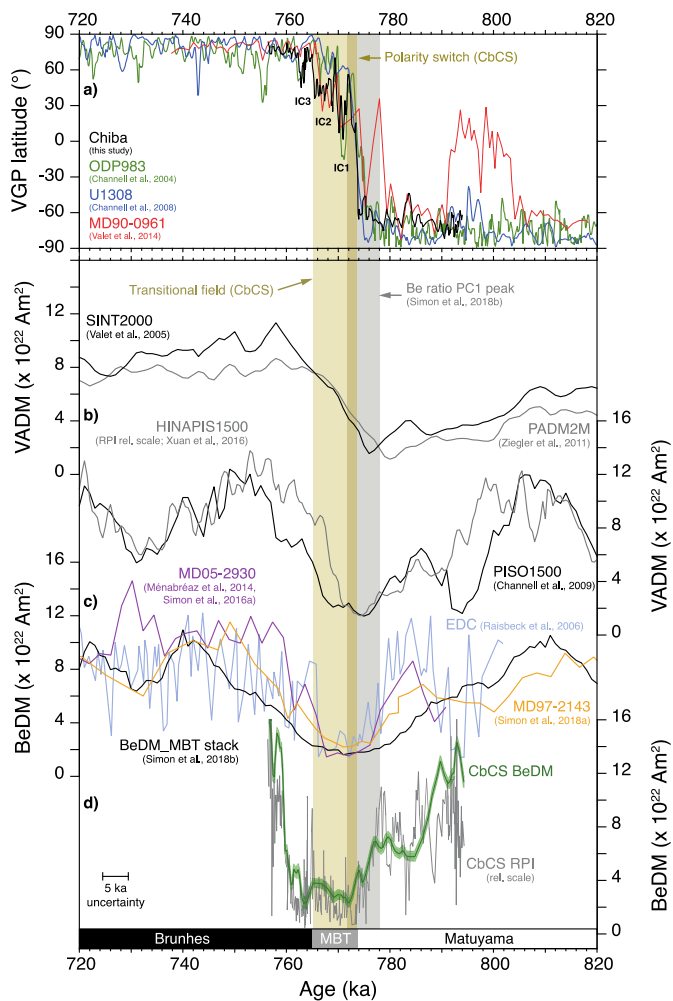


**Fig. 5.** Global comparison of the MBT record. (a) VGP from CbCS (black), IODP site U1308 (blue), ODP983 (green), and MD90-0961 (red). (b) Virtual axial dipole moment (VADM) series from reference RPI stacks (Xuan et al., 2016) and (c) dipole moment series calibrated from  $^{10}\text{Be}$ -records (BeDM). The  $^{10}\text{Be}$ -flux from EDC (light blue, Raisbeck et al., 2006) has been calibrated in term of DM using the method from Simon et al. (2018b). (d) BeDM and RPI records from the CbCS.

tal dynamo (Fig. 5b; Valet et al., 2005; Guyodo and Valet, 2006; Leonhardt and Fabian, 2007; Pétrélis et al., 2009; Ziegler and Constable, 2011; Avery et al., 2017), supporting different physical control processes characterized by different timescales, i.e., long-term diffusion associated with field decay and rapid advection during recovery. Overall, the field decreases to its lowest values in about 18 ka, but it recovers through only a 3 ka period. During the transitional field interval, the succession of rapid instabilities (<1 ka) demonstrates complex field behaviors at the surface resulting from the rapid emergence, growth, and transport of reversed flux patches at the core–mantle boundary associated with strong advective processes in the fluid outer core resulting in broken equatorial flow symmetry (Bloxham and Gubbins, 1986; Coe et al., 2000; Amit et al., 2010; Olson et al., 2011).

The CbCS records a sequence of geomagnetic field instabilities coinciding with periods of low-dipole intensity during the MBT period. The actual record does not allow a comparison of these transitional features with secular variations during stable polarity intervals. Future sampling at this site might hold the keys for analyzing the two extremes of the geomagnetic field variability continuum, i.e., reversals and secular variations, and allow comparison of reversal values with long-time averages.

## 6. Conclusion

The coupling of two independent proxies, paleomagnetism and  $^{10}\text{Be}$ , provided evidence that the magnetization acquisition in the high-resolution CbCS conserved the timing of rapid geomagnetic features, allowing accurate interpretations of the paleomagnetic record of the Matuyama–Brunhes polarity transition. Our results revealed that transient directions correlated with an episode of geomagnetic dipole moment collapse and that the field experienced a sequence of rapid oscillations before the full polarity state was reestablished. A polarity switch (PS) episode from 771.9–773.9 ka capturing most of the angular deviation followed by a directional instability phase (IC1) until 768.5 ka occurred during weak dipole field. Four rapid episodes of directional instabilities preceding and following the PS–IC1 phase complete the reversal sequence. The asymmetry observed between the long-term dipole decay phase and the sharp recovery phase, and rapid oscillations (<1 ka) evidence the complex transitional field during the weak dipole field. The recognition of these features further emphasizes the fact that most reversal records do not integrate the full field behavior, which is problematic for reconstructing the precise dynamics and understanding the underlying physical processes. However, this shortcoming does not hamper stratigraphic correlations among most geologic records, especially when using a dipolar intensity proxy as the global marker.

## Acknowledgements

QS acknowledges Laëticia Gacem and Coralie Andreucci for assistance with the beryllium sample preparation. YS and MO were supported by a JSPS Kakenhi Grant (16H04068; 15K13581; 17H06321). James E.T. Channell is acknowledged for sharing North Atlantic paleomagnetic data. The ASTER AMS national facility (CEREGE, Aix en Provence) is supported by INSU/CNRS, ANR through the EQUIPEX “ASTER-CEREGE” action, and IRD. The data presented in this study are available within the supporting information.

## References

- Amit, H., Leonhardt, R., Wicht, J., 2010. Polarity reversals from paleomagnetic observations and numerical dynamo simulations. *Space Sci. Rev.* 155, 293–335. <https://doi.org/10.1007/s11214-010-9695-2>.
- Avery, M.S., Gee, J.S., Constable, C.G., 2017. Asymmetry in growth and decay of the geomagnetic dipole revealed in seafloor magnetization. *Earth Planet. Sci. Lett.* 467, 79–88. <https://doi.org/10.1016/j.epsl.2017.03.020>.
- Balbas, A.M., Koppers, A.A.P., Clark, P.U., Coe, R.S., Reilly, B.T., Stoner, S.J.S., Konrad, K., 2018. Millennial-scale instability in the geomagnetic field prior to the Matuyama–Brunhes reversal. *Geochem. Geophys. Geosyst.* 19, 952–967. <https://doi.org/10.1002/2017GC007404>.
- Bloxham, J., Gubbins, D., 1986. Geomagnetic field analysis—IV. Testing the frozen-flux hypothesis. *Geophys. J. R. Astron. Soc.* 84 (1), 139–152.
- Bourlès, D.L., Raisbeck, G.M., Yiou, F., 1989.  $^{10}\text{Be}$  and  $^9\text{Be}$  in Marine sediments and their potential for dating. *Geochim. Cosmochim. Acta* 53 (2), 443–452.
- Braucher, R., Guillou, V., Bourlès, D.L., Arnold, M., Aumaitre, G., Keddadouche, K., Nottoli, E., 2015. Preparation of ASTER in-house  $^{10}\text{Be}/^9\text{Be}$  standard solutions. *Nucl. Instrum. Methods Phys. Res., Sect. B, Beam Interact. Mater. Atoms* 361, 335–340.
- Buffett, B., 2015. Dipole fluctuations and the duration of geomagnetic polarity transitions. *Geophys. Res. Lett.* 42. <https://doi.org/10.1002/2015GL065700>.
- Carcaillet, J.T., Bourlès, D.L., Thouveny, N., Arnold, M., 2004. A high resolution authigenic  $^{10}\text{Be}/^9\text{Be}$  record of geomagnetic moment variations over the last 300 ka from sedimentary cores of the Portuguese margin. *Earth Planet. Sci. Lett.* 219 (3), 397–412. <https://doi.org/10.1016/S0012821X03007027>.
- Channell, J.E.T., Kleiven, H.F., 2000. Geomagnetic palaeointensities and astrochronological ages for the Matuyama–Brunhes boundary and the boundaries of the Jaramillo subchron: palaeomagnetic and oxygen isotope records from ODP site 983. *Philos. Trans. R. Soc. Lond., Ser. A* 358 (1768), 1027–1047.
- Channell, J.E.T., Hodell, D.A., Xuan, C., Mazaud, A., Stoner, J.S., 2008. Age calibrated relative paleointensity for the last 1.5 Myr at IODP Site U1308 (North Atlantic). *Earth Planet. Sci. Lett.* 274, 59–71.

- Channell, J.E.T., Xuan, C., Hodell, D.A., 2009. Stacking paleointensity and oxygen isotope data for the last 1.5 Myr (PISO-1500). *Earth Planet. Sci. Lett.* 283, 14–23.
- Channell, J.E.T., Hodell, D.A., Singer, B.S., Xuan, C., 2010. Reconciling astrochronological and  $^{40}\text{Ar}/^{39}\text{Ar}$  ages for the Matuyama-Brunhes boundary in the late Matuyama Chron. *Geochim. Geophys. Geosyst.* 11, Q0AA12. <https://doi.org/10.1029/2010GC003203>.
- Channell, J.E.T., 2017. Complexity in Matuyama–Brunhes polarity transitions from North Atlantic IODP/ODP deep-sea sites. *Earth Planet. Sci. Lett.* 467, 43–56.
- Chmeleff, J., von Blanckenburg, F., Kossert, K., Jakob, D., 2010. Determination of the  $^{10}\text{Be}$  half-life by multicollector ICP-MS and liquid scintillation counting. *Nucl. Instrum. Methods Phys. Res. B* 268 (2), 192–199. <https://doi.org/10.1016/j.nimb.2009.09.012>.
- Chou, Y.M., Jiang, X., Liu, Q., Hu, H.M., Wu, C.C., Liu, J., Jiang, Z., Lee, T.Q., Wang, C.C., Song, Y.F., Chaing, C.C., Tan, L., Lone, M.A., Pann, Y., Zhu, R., He, Y., Chou, Y.C., Tan, A.H., Roberts, A.P., Zhao, X., Shen, C.C., 2018. Multidecadally resolved polarity oscillations during a geomagnetic excursion. *Proc. Natl. Acad. Sci. USA* 115 (36), 8913–8918. <https://doi.org/10.1073/pnas.1720404115>.
- Clement, B.M., 2004. Dependence of the duration of geomagnetic polarity reversals on site latitude. *Nature* 428, 637–640.
- Coe, R.S., Glen, J.M.G., 2004. The complexity of reversals. In: Channell, J.E.T., et al. (Eds.), *Timescales of the Paleomagnetic Field*. In: Geophysical Monograph Series, vol. 145. American Geophysical Union, Washington, DC, pp. 221–232.
- Coe, R.S., Hongre, L., Glatzmaier, G.A., 2000. An examination of simulated geomagnetic reversals from a paleomagnetic perspective. *Philos. Trans. R. Soc. Lond. A* 358, 1141–1170.
- Du, Y., Zhou, W., Xian, F., Qiang, X., Kong, X., Zhao, G., Xie, X., Fu, Y., 2018.  $^{10}\text{Be}$  signature of the Matuyama-Brunhes transition from the Heqing paleolake basin. *Quat. Sci. Rev.* 199, 41–48.
- Elderfield, H., Ferretti, P., Greaves, M., Crowhurst, S., McCave, I.N., Hodell, D., Piotrowski, A.M., 2012. Evolution of ocean temperature and ice volume through the mid-Pleistocene climate transition. *Science* 337, 704–709. <https://doi.org/10.1126/science.1221294>.
- Evans, M.E., Muxworthy, A.R., 2018. A re-appraisal of the proposed rapid Matuyama-Brunhes geomagnetic reversal in the Sulmona Basin, Italy. *Geophys. J. Int.* <https://doi.org/10.1093/gji/ggy111>.
- Finlay, C.C., Aubert, J., Gillet, N., 2016. Gyre-driven decay of the Earth's magnetic dipole. *Nat. Commun.* 7, 10422. <https://doi.org/10.1038/ncomms10422>.
- Frank, M., Schwarz, B., Baumann, S., Kubik, P.W., Suter, M., Mangini, A., 1997. A 200 kyr record of cosmogenic radionuclide production rate and geomagnetic field intensity from  $^{10}\text{Be}$  in globally stacked deep-sea sediments. *Earth Planet. Sci. Lett.* 149 (1–4), 121–129.
- Genevey, A., Gallet, Y., Constable, C.G., Korte, M., Hulot, G., 2008. Archeoint: an upgraded compilation of geomagnetic field intensity data for the past ten millennia and its application to the recovery of the past dipole moment. *Geochim. Geophys. Geosyst.* 9, Q04038. <https://doi.org/10.1029/2007GC001881>.
- Guyodo, Y., Valet, J.P., 2006. A comparison of relative paleointensity records of the Matuyama Chron for the period 0.75–1.25 Ma. *Phys. Earth Planet. Inter.* 156, 205–212.
- Hartl, P., Tauxe, L., 1996. A precursor to the Matuyama/Brunhes transition-field instability as recorded in pelagic sediments. *Earth Planet. Sci. Lett.* 138, 121–135.
- Horiuchi, K., Kamata, K., Maejima, S., Sasaki, S., Sasaki, N., Yamazaki, T., Fujita, S., Motoyama, H., Matsuzaki, H., 2016. Multiple  $^{10}\text{Be}$  records revealing the history of cosmic-ray variations across the Iceland Basin excursion. *Earth Planet. Sci. Lett.* 440, 105–114.
- Hyodo, M., Biawas, D.K., Noda, T., Tomioka, N., Mishima, T., Itota, C., Sato, H., 2006. Millennial- to submillennial-scale features of the Matuyama-Brunhes geomagnetic polarity transition from Osaka Bay, southwestern Japan. *J. Geophys. Res., Solid Earth* 111. <https://doi.org/10.1029/2004JB003584>.
- Jarboe, N.A., Coe, R.S., Glen, J.M.G., 2011. Evidence from lava flows for complex polarity transitions: the new composite Steens mountain reversal record. *Geophys. J. Int.* 186 (2), 580–602.
- Kazaoka, O., Sugauma, Y., Okada, M., Kameo, K., Head, M.J., Yoshida, T., Kameyama, S., Nirei, H., Aida, N., Kumai, H., 2015. Stratigraphy of the Kazusa Group, Boso Peninsula: an expanded and highly-resolved marine sedimentary record from the Lower and Middle Pleistocene of central Japan. *Quat. Int.* 383, 116–135.
- Kirscher, U., Winkhofer, M., Hackl, M., Bachtadse, V., 2018. Detailed Jaramillo field reversals recorded in lake sediments from Armenia – lower mantle influence on the magnetic field revisited. *Earth Planet. Sci. Lett.* 484, 124–134.
- Korschinek, G., Bergmaier, A., Faestermann, T., Gerstmann, U.C., Knie, K., Rugel, G., Wallner, A., Dillmann, I., Dollinger, G., Lierse von Gostomski, Ch., Kossert, K., Maiti, M., Poutivtsev, M., Rimmert, A., 2010. A new value for the half-life of  $^{10}\text{Be}$  by Heavy-Ion Elastic Recoil Detection and liquid scintillation counting. *Nucl. Instrum. Methods Phys. Res. B* 268 (2), 187–191. <https://doi.org/10.1016/j.nimb.2009.09.020>.
- Kusu, C., Okada, M., Nozaki, A., Majima, R., Wada, H., 2016. A record of the upper Olduvai geomagnetic polarity transition from a sediment core in southern Yokohama City, Pacific side of central Japan. *Prog. Earth Planet. Sci.* 3, 26. <https://doi.org/10.1186/s40645-016-0104-7>.
- Laj, C., Kissel, C., 2015. An impending geomagnetic transition? Hints from the past. *Front. Earth Sci.* 3, 61. <https://doi.org/10.3389/feart.2015.00061>.
- Lal, D., Peters, B., 1967. Cosmic ray produced radioactivity on the Earth. In: *Handbuch der Physik*, vol. XLVI/2. Springer, New York, pp. 551–612.
- Leonhardt, R., Fabian, K., 2007. Paleomagnetic reconstruction of the global geomagnetic field evolution during the Matuyama/Brunhes transition: iterative Bayesian inversion and independent verification. *Earth Planet. Sci. Lett.* 253 (1), 172–195.
- Love, J.J., Mazaud, A., 1997. A database for the Matuyama-Brunhes magnetic reversal. *Phys. Earth Planet. Inter.* 103 (3), 207–245.
- Mazaud, A., Channell, J.E.T., 1999. The top Olduvai polarity transition at ODP Site 983 (Iceland Basin). *Earth Planet. Sci. Lett.* 166, 1–13. <https://doi.org/10.1029/2001JB000491>.
- Mazaud, A., Channell, J.E.T., Xuan, C., Stoner, J.S., 2009. Upper and lower Jaramillo polarity transitions recorded in IODP Expedition 303 North Atlantic sediments: implications for transitional field geometry. *Phys. Earth Planet. Inter.* 172 (3), 131–140.
- Ménabréaz, L., Bourlès, D.L., Thouveny, N., 2012. Amplitude and timing of the Laschamp geomagnetic dipole low from the global atmospheric  $^{10}\text{Be}$  overproduction: contribution of authigenic  $^{10}\text{Be}/^9\text{Be}$  ratios in west equatorial Pacific sediments. *J. Geophys. Res.* 117 (B11101).
- Ménabréaz, L., Thouveny, N., Bourlès, D.L., Vidal, L., 2014. The geomagnetic dipole moment variation between 250 and 800 ka BP reconstructed from the authigenic  $^{10}\text{Be}/^9\text{Be}$  signature in West Equatorial Pacific sediments. *Earth Planet. Sci. Lett.* 385, 190–205.
- Merrill, R.T., McFadden, P.L., 1999. Geomagnetic polarity transitions. *Rev. Geophys.* 37 (2), 201–226.
- Mochizuki, N., Oda, H., Ishizuka, O., Yamazaki, T., Tsunakawa, H., 2011. Paleointensity variation across the Matuyama-Brunhes polarity transition: observations from lavas at Punaruu Valley, Tahiti. *J. Geophys. Res.* 116, B06103. <https://doi.org/10.1029/2010JB008093>.
- Morzfeld, M., Fournier, A., Hulot, G., 2017. Coarse predictions of dipole reversals by low-dimensional modeling and data assimilation. *Phys. Earth Planet. Inter.* 262, 8–27.
- Nomade, S., Bassinot, F., Marino, M., Simon, Q., Dewilde, F., Maiorano, P., Isguder, G., Blamart, D., Girone, A., Scao, V., Pereira, A., Toti, F., Bertini, A., Combourieu-Nebout, N., Peral, C., Bourles, D.L., Petrosino, P., Gallicchio, S., Ciaranfi, N., 2019. High-resolution foraminifer stable isotope record of MIS 19 at Montalbano Jonico, southern Italy: a window into Mediterranean climatic variability during a low-eccentricity interglacial. *Quat. Sci. Rev.* 205, 106–125.
- Nowaczyk, N.R., Arz, H.W., Frank, U., Kind, J., Plessen, B., 2012. Dynamics of the Laschamp geomagnetic excursion from Black Sea sediments. *Earth Planet. Sci. Lett.* 351–352, 54–69.
- Okada, M., Niitsuma, N., 1989. Detailed paleomagnetic records during the Brunhes–Matuyama geomagnetic reversal and a direct determination of depth lag for magnetization in marine sediments. *Phys. Earth Planet. Inter.* 56, 133–150.
- Okada, M., Sugauma, Y., Haneda, Y., Kazaoka, O., 2017. Paleomagnetic direction and paleointensity variations during the Matuyama-Brunhes polarity transition from a marine succession in the Chiba composite section of the Boso Peninsula, central Japan. *Earth Planets Space* 69, 45. <https://doi.org/10.1186/s40623-017-0627-1>.
- Olson, P.L., Glatzmaier, G.A., Coe, R.S., 2011. Complex polarity reversals in a geodynamo model. *Earth Planet. Sci. Lett.* 304, 168–179.
- Pavón-Carrasco, F.J., Osete, M.L., Torta, J.M., De Santis, A., 2014. A geomagnetic field model for the Holocene based on archeomagnetic and lava flow data. *Earth Planet. Sci. Lett.* 388, 98–109.
- Pétrellis, F., Fauve, S., Dormy, E., Valet, J.P., 2009. Simple mechanism for reversals of Earth's magnetic field. *Phys. Rev. Lett.* 102, 144503.
- Pickering, K.T., Souter, C., Oba, T., Taira, A., Schaaf, M., Platzman, E., 1999. Glacioeustatic control on deep-marine clastic forearc sedimentation, Pliocene–mid-Pleistocene (c. 1180–600 ka) Kazusa Group, SE Japan. *J. Geol. Soc.* 156, 125–136.
- Poluianov, S.V., Kovaltsov, G.A., Mishev, A.L., Usoskin, I.G., 2016. Production of cosmogenic isotopes  $^7\text{Be}$ ,  $^{10}\text{Be}$ ,  $^{14}\text{C}$ ,  $^{22}\text{Na}$ , and  $^{36}\text{Cl}$  in the atmosphere: altitudinal profiles of yield functions. *J. Geophys. Res., Atmos.* 121, 8125–8136. <https://doi.org/10.1002/2016JD025034>.
- Quidelleur, X., Valet, J.P., Thouveny, N., 1992. Multicomponent magnetization in paleomagnetic records of reversals from continental sediments in Bolivia. *Earth Planet. Sci. Lett.* 111, 23–39.
- Raisbeck, G.M., Yiou, F., Bourlès, D., Kent, D.V., 1985. Evidence for an increase in cosmogenic  $^{10}\text{Be}$  during a geomagnetic reversal. *Nature* 315, 315–317. <https://doi.org/10.1038/315315a0>.
- Raisbeck, G.M., Yiou, F., Cattani, O., Jouzel, J., 2006.  $^{10}\text{Be}$  evidence for the Matuyama–Brunhes geomagnetic reversal in the EPICA Dome C ice core. *Nature* 444 (7115), 82–84.
- Ricci, J., Carlut, J., Valet, J.P., 2018. Paleosecular variation recorded by Quaternary lava flows from Guadeloupe Island. *Sci. Rep.* 8, 10147. <https://doi.org/10.1038/s41598-018-28384-z>.
- Roberts, A.P., Winkhofer, M., 2004. Why are geomagnetic excursions not always recorded in sediments? Constraints from post-depositional remanent magnetization lock-in modelling. *Earth Planet. Sci. Lett.* 227, 345–359.
- Roberts, A.P., Florindo, F., Larrasoana, J.C., O'Regan, M.A., Zhao, X., 2010. Complex polarity pattern at the (former) Plio-Pleistocene global stratotype section at Vrica (Italy): remagnetization by magnetic iron sulphides. *Earth Planet. Sci. Lett.* 292, 98–111.

- Sagnotti, L., Cascella, A., Ciaranfi, N., Macrí, P., Maiorano, P., Marino, M., Taddeucci, J., 2010. Rock magnetism and palaeomagnetism of the Montalbano Jonico section (Italy): evidence for late diagenetic growth of greigite and implications for magnetostratigraphy. *Geophys. J. Int.* 180, 1049–1066.
- Sagnotti, L., Giaccio, B., Liddicoat, J.C., Nomade, S., Renne, P.R., Scardia, G., Sprain, C.J., 2016. How fast was the Matuyama–Brunhes geomagnetic reversal? A new subcentennial record from the Sulmona Basin, central Italy. *Geophys. J. Int.* 204, 798–812. <https://doi.org/10.1093/gji/ggv486>.
- Simon, Q., Thouveny, N., Bourlès, D.L., Valet, J.-P., Bassinot, F., Ménabréaz, L., Guillou, V., Choy, S., Beaufort, L., 2016a. Authigenic  $^{10}\text{Be}/^9\text{Be}$  ratio signatures of the cosmogenic nuclide production linked to geomagnetic dipole moment variation since the Brunhes/Matuyama boundary. *J. Geophys. Res.* 121, 7716–7741. <https://doi.org/10.1002/2016JB013335>.
- Simon, Q., Thouveny, N., Bourlès, D.L., Nuttin, L., St-Onge, G., Hillaire-Marcel, C., 2016b. Authigenic  $^{10}\text{Be}/^9\text{Be}$  ratios and  $^{10}\text{Be}$ -fluxes ( $^{230}\text{Th}_{\text{xs}}$ -normalized) in central Baffin Bay during the last glacial cycle: paleoenvironmental implications. *Quat. Sci. Rev.* 140, 142–162.
- Simon, Q., Bourlès, D.L., Bassinot, F., Nomade, S., Marino, M., Ciaranfi, N., Girone, A., Maiorano, P., Thouveny, N., Choy, S., Dewilde, F., Scao, V., Isguder, G., Blamart, D., 2017. Authigenic  $^{10}\text{Be}/^9\text{Be}$  ratio signature of the Matuyama–Brunhes boundary in the Montalbano Jonico marine succession. *Earth Planet. Sci. Lett.* 460, 255–267. <https://doi.org/10.1016/j.epsl.2016.11.052>.
- Simon, Q., Bourlès, D.L., Thouveny, N., Horng, C.-S., Valet, J.-P., Bassinot, F., Choy, S., 2018a. Cosmogenic signature of geomagnetic reversals and excursions from the Réunion event to the Matuyama–Brunhes transition (0.7–2.14 Ma interval). *Earth Planet. Sci. Lett.* 482, 510–524. <https://doi.org/10.1016/j.epsl.2017.11.021>.
- Simon, Q., Thouveny, N., Bourlès, D.L., Bassinot, F., Savranskaia, T., Valet, J.-P., 2018b. Increased production of cosmogenic  $^{10}\text{Be}$  recorded in oceanic sediment sequences: information on the age, duration, and amplitude of the geomagnetic dipole moment minimum over the Matuyama–Brunhes transition. *Earth Planet. Sci. Lett.* 489, 191–202. <https://doi.org/10.1016/j.epsl.2018.02.036>.
- Singer, B.S., Hoffman, K.A., Coe, R.S., Brown, L.L., Jicha, B.R., Pringle, M.S., Chauvin, A., 2005. Structural and temporal requirements for geomagnetic field reversal deduced from lava flows. *Nature* 434, 633–636.
- Singer, B.S., Jicha, B.R., Mochizuki, N., Coe, R.S., 2018. Synchronizing volcanic, sedimentary, and ice core records of Earth's last magnetic polarity reversal. In: AGU Fall Meeting in Washington, D.C., USA. Paper No. 353957. <https://agu.confex.com/agu/fm18/meetingapp.cgi/Paper/353957>.
- Suganuma, Y., Yokoyama, Y., Yamazaki, T., Kawamura, K., Horng, C.-S., Matsuzaki, H., 2010.  $^{10}\text{Be}$  evidence for delayed acquisition of remanent magnetization in marine sediments: implication for a new age for the Matuyama–Brunhes boundary. *Earth Planet. Sci. Lett.* 296, 443–450. <https://doi.org/10.1016/j.epsl.2010.05.031>.
- Suganuma, Y., Okuno, J., Heslop, D., Roberts, A.P., Yamazaki, T., Yokoyama, Y., 2011. Post-depositional remanent magnetization lock-in for marine sediments deduced from  $^{10}\text{Be}$  and paleomagnetic records through the Matuyama–Brunhes boundary. *Earth Planet. Sci. Lett.* 311, 39–52.
- Suganuma, Y., Okada, M., Horie, K., Kaiden, H., Takehara, M., Senda, R., Kimura, J., Haneda, Y., Kawamura, K., Kazaoka, O., Head, M.J., 2015. Age of Matuyama–Brunhes boundary constrained by U–Pb zircon dating of a widespread tephra. *Geology* 43, 491–494.
- Suganuma, Y., Haneda, Y., Kameo, K., Kubota, Y., Hayashi, H., Itaki, T., Okuda, M., Head, M.J., Sugaya, M., Nakazato, H., Igarashi, A., Shikoku, K., Hongo, M., Watanabe, M., Satoguchi, Y., Takeshita, Y., Nishida, N., Izumi, K., Kawamura, K., Kawamata, M., Okuno, J., Yoshida, T., Ogitsu, I., Yabusaki, H., Okada, M., 2018. Paleoclimatic and paleoceanographic records of Marine Isotope Stage 19 at the Chiba composite section, central Japan: a reference for the Early–Middle Pleistocene boundary. *Quat. Sci. Rev.* 191, 406–430.
- Takeshita, Y., Matsushima, N., Teradaira, H., Uchiyama, T., Kumai, H., 2016. A marker tephra bed close to the Middle Pleistocene boundary: distribution of the Ontake–Byakubi tephra in central Japan. *Quat. Int.* 397, 27–38. <https://doi.org/10.1016/j.quaint.2015.03.054>.
- Tauxe, L., 1993. Sedimentary records of relative paleointensity of the geomagnetic field: theory and practice. *Rev. Geophys.* 31, 319–354. <https://doi.org/10.1029/93RG01771>.
- Tauxe, L., Hebert, T., Shackleton, N.J., Kok, Y.S., 1996. Astronomical calibration of the Matuyama–Brunhes boundary: consequences for magnetic remanence acquisition in marine carbonates and the Asian loess sequences. *Earth Planet. Sci. Lett.* 140, 133–146.
- Thouveny, N., Bourlès, D.L., Saracco, G., Carcaillet, J.T., Bassinot, F., 2008. Paleoclimatic context of geomagnetic dipole lows and excursions in the Brunhes, clue for an orbital influence on the geodynamo? *Earth Planet. Sci. Lett.* 275 (3–4), 269–284. <https://doi.org/10.1016/j.epsl.2008.08.020>.
- Tric, E., Laj, C., Valet, J.-P., Tucholka, P., Paterne, M., Guichard, F., 1991. The Blake geomagnetic event: transition geometry, dynamical characteristics and geomagnetic significance. *Earth Planet. Sci. Lett.* 102, 1–13.
- Valet, J.P., 2003. Time variations in geomagnetic intensity. *Rev. Geophys.* 41 (1), 1004. <https://doi.org/10.1029/2001RG000104>.
- Valet, J.P., Meynadier, L., Guyodo, Y., 2005. Geomagnetic field strength and reversal rate over the past 2 million years. *Nature* 435, 802–805.
- Valet, J.P., Fournier, A., Courtillot, V., Herrero-Bervera, E., 2012. Dynamical similarity of geomagnetic field reversals. *Nature* 490, 89–94. <https://doi.org/10.1038/nature11491>.
- Valet, J.P., Bassinot, F., Bouilloux, A., Bourlès, D.L., Nomade, S., Guillou, V., Lopes, F., Thouveny, N., Dewilde, F., 2014. Geomagnetic, cosmogenic and climatic changes across the last geomagnetic reversal from Equatorial Indian Ocean sediments. *Earth Planet. Sci. Lett.* 397, 67–79. <https://doi.org/10.1016/j.epsl.2014.03.053>.
- Valet, J.P., Meynadier, L., Simon, Q., Thouveny, N., 2016. When and why sediments fail to record the geomagnetic field during polarity reversals? *Earth Planet. Sci. Lett.* 453, 96–107.
- Valet, J.P., Fournier, A., 2016. Deciphering records of geomagnetic reversals. *Rev. Geophys.* 54. <https://doi.org/10.1002/2015RG000506>.
- Valet, J.P., Bassinot, F., Simon, Q., Savranskaia, T., Thouveny, N., Bourlès, D.L., Villedieu, A., 2019. Constraining the age of the last geomagnetic reversal from geochemical and magnetic analyses of Atlantic, Indian, and Pacific Ocean sediments. *Earth Planet. Sci. Lett.* 506, 323–331.
- Xuan, C., Channell, J.E.T., Hodell, D.A., 2016. Quaternary magnetic and oxygen isotope stratigraphy in diatom-rich sediments of the southern Gardar Drift (IODP Site U1304, North Atlantic). *Quat. Sci. Rev.* 142, 74–89.
- Ziegler, L.B., Constable, C.C., 2011. Asymmetry in growth and decay of the geomagnetic dipole. *Earth Planet. Sci. Lett.* 312, 300–304.